

Edge dependent Josephson diode effect in WTe_2-based Josephson junction

Guo-Liang Guo(郭国良), Xiao-Hong Pan(潘晓红), Hao Dong(董豪), Xin Liu(刘鑫)

Citation: Chin. Phys. B. 35, 097401 (2026). DOI: 10.1088/1674-1056/ae6d9d |
CSTR: 32038.14.CPB.ae6d9d
http://cpb.iphy.ac.cn; http://iopscience.iop.org/cpb

What follows is a list of articles you may be interested in

Multiple surface states, nontrivial band topology, and antiferromagnetism in $GdAuAl_4Ge_2$

Chengcheng Zhang(张成成), Yuan Wang(王渊), Fayuan Zhang(张发远), Hongtao Rong(戎洪涛), Yongqing Cai(蔡永青), Le Wang(王乐), Xiao-Ming Ma(马小明), Shu Guo(郭抒), Zhongjia Chen(陈仲佳), Yanan Wang(王亚南), Zhicheng Jiang(江志诚), Yichen Yang(杨逸尘), Zhengtai Liu(刘正太), Mao Ye(叶茂), Junhao Lin(林君浩), Jiawei Mei(梅佳伟), Zhanyang Hao(郝占阳), Zijuan Xie(谢子娟), Chaoyu Chen(陈朝宇)
Chin. Phys. B. 32, 077401 (2023). DOI: 10.1088/1674-1056/acca0e

Ac Josephson effect in Corbino-geometry Josephson junctions constructed on Bi_2Te_3 surface

Yunxiao Zhang(张云潇), Zhaozheng Lyu(吕昭征), Xiang Wang(王翔), Enna Zhuo(卓恩娜), Xiaopei Sun(孙晓培), Bing Li(李冰), Jie Shen(沈洁), Guangtong Liu(刘广同), Fanming Qu(屈凡明), Li Lü(吕力)
Chin. Phys. B. 31, 107402 (2022). DOI: 10.1088/1674-1056/ac89d4

Probing the minigap in topological insulator-based Josephson junctions under radio frequency irradiation

Guang Yang(杨光), Zhaozheng Lyu(吕昭征), Xiang Zhang(张祥), Fanming Qu(屈凡明), Li Lu(吕力)
Chin. Phys. B. 28, 127402 (2019). DOI: 10.1088/1674-1056/ab5211

Giant enhancement of superconductivity in few layers $MoTe_2$

Yuan Gan(甘远), Chang-Woo Cho, Alei Li(李阿蕾), Jian Lyu(吕坚), Xu Du(杜序), Jin-Sheng Wen(温锦生), Li-Yuan Zhang(张立源)
Chin. Phys. B. 28, 117401 (2019). DOI: 10.1088/1674-1056/ab457f

Topological superconductivity in a $Bi_2Te_3/NbSe_2$ heterostructure: A review

Hao Zheng(郑浩), Jin-Feng Jia(贾金锋)
Chin. Phys. B. 28, 067403 (2019). DOI: 10.1088/1674-1056/28/6/067403

Edge dependent Josephson diode effect in WTe_2-based Josephson junction

Guo-Liang Guo(郭国良)[1,2,3,†], Xiao-Hong Pan(潘晓红)[4], Hao Dong(董豪)[5], and Xin Liu(刘鑫)[1,2,3,5,6,‡]

[1] *Shanghai Research Center for Quantum Sciences, Shanghai* 201315, *China*
[2] *Tsung-Dao Lee Institute, Shanghai Jiao Tong University, Shanghai* 201210, *China*
[3] *School of Physics and Astronomy, Shanghai Jiao Tong University, Shanghai* 200240, *China*
[4] *Department of Physics, College of Physics, Optoelectronic Engineering, Jinan University, Guangzhou* 510632, *China*
[5] *School of Physics and Wuhan National High Magnetic Field Center, Huazhong University of Science and Technology, Wuhan* 430074, *China*
[6] *Hefei National Laboratory, Hefei* 230088, *China*

(Received 16 April 2026; revised manuscript received 8 May 2026; accepted manuscript online 14 May 2026)

The Josephson diode effect (JDE), a nonreciprocal supercurrent, is a cornerstone for future dissipationless electronics, yet achieving high efficiency in a simple device architecture remains a significant challenge. Here, we theoretically investigate the JDE in a junction based on monolayer 1T′-WTe_2. We first establish that different edge terminations of a WTe_2 nanoribbon lead to diverse electronic band structures, some of which host asymmetric edge states even with crystallographically equivalent terminations. This intrinsic asymmetry provides a natural platform for realizing the JDE. With a WTe_2-based Josephson junction, we demonstrate a significant JDE arising purely from these asymmetric edges when time-reversal symmetry is broken by a magnetic flux. While the efficiency of this edge-state-driven JDE is inherently limited, we discover a crucial mechanism for its enhancement: by tuning the chemical potential into the bulk bands, the interplay between edge and bulk transport channels boosts the maximum diode efficiency more than 50%. To interpret and rationalize these trends, we construct a minimal theoretical model for the Josephson potential that captures edge–bulk interference and quantitatively explains the numerical dependence on magnetic flux, chemical potential, and device geometry. Furthermore, we show that this enhanced JDE is robust against moderate edge disorder. Our findings not only propose a novel route to achieve a highly efficient JDE using intrinsic material properties but also highlight the potential of engineered WTe_2 systems for developing advanced superconducting quantum devices.

Keywords: Josephson diode effect, topological insulators, Josephson junctions, edge states

PACS: 74.45.+c, 78.20.Bh ,85.30.Kk

DOI: 10.1088/1674-1056/ae6d9d **CSTR:** 32038.14.CPB.ae6d9d

1. Introduction

The semiconductor diode, whose foundational operating principles stem from the seminal p–n junction,[1,2] constitutes an indispensable class of electronic components with ubiquitous technological implementations. A conceptually analogous yet physically distinct phenomenon emerges in superconductors (SC), a phenomenon known as the superconducting diode effect (SDE), which allows the superconducting current to flow only in one direction.[3] This nonreciprocal supercurrent phenomenon has garnered substantial experimental and theoretical attention in contemporary condensed matter physics,[4–17] due to its revelation of novel transport mechanisms in symmetry-broken superconducting systems, and its potential for unprecedented device integration prospects. This asymmetric supercurrent rectification differs fundamentally from conventional semiconductor diode operation, enabling innovative dissipationless electronics that could potentially revolutionize superconducting circuit design. In superconducting systems, Josephson junctions and superconducting quantum interference devices (SQUIDs) are the typical superconducting devices.[18,19] The nonreciprocal supercurrent effect in Josephson junctions is then termed the Josephson diode effect (JDE),[20–27] which has different magnitudes of critical currents ($|I_{c+}| \neq |I_{c-}|$) in opposite directions. This has been experimentally realized and theoretically calculated in various systems with broken time-reversal and inversion symmetries.[14–16] The time-reversal symmetry breaking is usually achieved by applying an external magnetic field,[28–33] while the inversion symmetry breaking can arise from the asymmetry of stacked heterostructures,[6,21] artificial device configuration,[34,35] interface,[36] and intrinsic lattice structure.[11,37] Furthermore, the field-free JDE has also been explored in various systems where the time-reversal symmetry is spontaneously broken by valley polarization,[38–40] (anti)ferromagnetic materials,[41,42] loop currents,[43] and exotic pairing function induced in unconventional superconductors.[44,45] Moreover, the JDE can also be realized in asymmetric supercurrent interferometers or

†Corresponding author. E-mail: sjtu2459870@sjtu.edu.cn
‡Corresponding author. E-mail: phyliuxin@sjtu.edu.cn

© 2026 Chinese Physical Society and IOP Publishing Ltd. All rights, including for text and data mining, AI training, and similar technologies, are reserved.

SQUID-like devices.[46–49] However, the diode efficiency $\eta = (I_{c+} - |I_{c-}|)/(I_{c+} + |I_{c-}|)$ is usually low[6,22,36] or the device is complex with more than one Josephson junction to gain the large diode efficiency.[46,47] On the other hand, the emergent discovery and technological implementation of novel material systems exhibiting exotic quantum phenomena has become a hallmark of modern condensed matter physics, with paradigmatic examples including (anti)ferromagnetism,[50,51] altermagnetism,[52,53] and topological surface states and edge states,[54–59] as well as boundary sublattice physics,[60,61] etc. Additionally, transition metal dichalcogenides (TMDs) are at the forefront of condensed matter research, as they host a rich variety of intriguing ground states, such as topological insulators (TI) and semimetals,[62,63] charge density waves,[64,65] and various types of possibly unconventional superconductivity.[66–68] This fundamental progress is predicated upon systematic investigations that establish viable pathways toward the realization of JDE and robust property optimization (including key performance metrics such as diode efficiency) in engineered quantum systems.

In this work, we propose to implement the JDE in 1T′-WTe_2 based Josephson junction utilizing external magnetic flux. The 2D 1T′-WTe_2 functions as a quantum spin Hall material characterized by strong crystalline anisotropy.[62] With 1T′-WTe_2 based Josephson junction, we demonstrate distinct edge-state ensembles due to varying edge-site atomic configurations (Fig. 1(a)), thereby enabling JDE through asymmetric SQUID-like geometric configurations in the presence of magnetic flux. The Josephson diode polarity (the sign of the diode efficiency) is contingent upon the magnitude of the magnetic flux and edge configurations. Crucially, we found that the maximal magnitude of diode efficiency can be enhanced to more than 53% when the Fermi surface is tuned to the bulk with the asymmetric edge states maintained (Fig. 1(c)). Finally, we find that edge disorder in the system has little effect on the large JDE. Our work provides a new material platform to achieve JDE with large diode efficiency and demonstrates a great potential of future applications.

2. Termination-dependent dispersion in the WTe_2

WTe_2 is one of the transition metal dichalcogenide (TMDC) materials known for its variety of polytypic structures, 2H, 1T, and 1T′.[62] The 2H structure, identified as a trivial semiconductor,[62] consists of three planes of hexagonally packed atoms in two dimensions, Te–W–Te, arranged in an ABA stacking pattern. Conversely, the 1T structure entails three planes with ABC stacking; however, it is unstable,[62] and undergoes lattice distortion along the x-direction, resulting in the stable 1T′ structure with a rectangular unit cell (Fig. 1(b)). For clarity, only the four atoms that contribute significantly to the low-energy bands near the Fermi level are shown; two Te atoms with negligible weight near the Fermi level are omitted. This distortion renders the lattice nonsymmorphic with the glide-mirror M_x and twofold rotation symmetry,[69–71] each accompanied by a half lattice translation in the x-direction (Fig. 1(b)). The unit cell structure also respects inversion symmetry. The monolayer 1T′ configuration of WTe_2 is known as the topological nontrivial phase with a band inversion at the Γ point.[72,73]

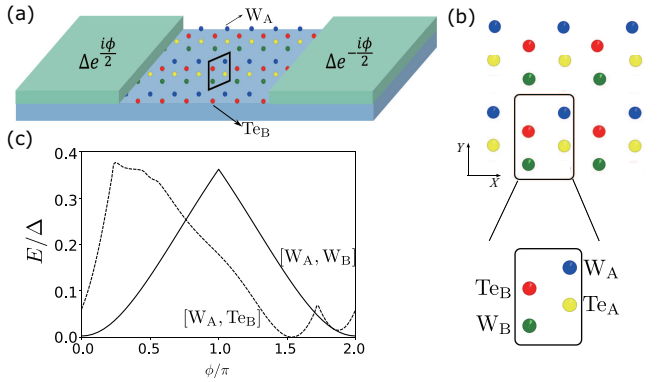


Fig. 1. (a) The setup of 1T′ WTe_2 based Josephson junction with the termination $[W_A, Te_B]$. (b) Lattice structure and unit cell of monolayer WTe_2. The colored circles indicate Wannier functions contributing to the low-energy physics. (c) The Josephson potential with the maximal diode efficiency (dashed line) with the inequivalent edges, and the Josephson potential with no diode effect (solid line) with the equivalent edges.

To investigate the JDE in the 1T′ WTe_2 based Josephson junction, we begin with the tight-binding (TB) model based on DFT calculations.[69,70] The four bands closest to the Fermi level originate from the two $d_{x^2-y^2}$-type orbitals of the W atoms and two p_x-type orbitals of the Te atoms. The Hamiltonian, based on the spin and four Wannier orbitals, is expressed as

$$H_0(k) = [h_0(k) - \mu] \otimes s_0 + V_{\mathrm{SOC}} \rho_z \tau_y s_z, \tag{1}$$

where ρ, τ, s label the $(W, Te)_i$ $(i = \mathrm{A}, \mathrm{B})$ sublattices, Wannier orbitals p, d and spin degree of freedom. The explicit form for the spin-degenerate part $h_0(k)$ is

$$h_0(k) = \begin{pmatrix} \varepsilon_{\mathrm{d}} & 0 & t_{\mathrm{d}}^{\mathrm{AB}} g_k & t_0^{\mathrm{AB}} f_k \\ 0 & \varepsilon_{\mathrm{p}} & -t_0^{\mathrm{AB}} f_k & t_{\mathrm{p}}^{\mathrm{AB}} g_k \\ t_{\mathrm{d}}^{\mathrm{AB}} g_k^* & -t_0^{\mathrm{AB}} f_k^* & \varepsilon_{\mathrm{d}} & 0 \\ t_0^{\mathrm{AB}} f_k^* & t_{\mathrm{p}}^{\mathrm{AB}} g_k^* & 0 & \varepsilon_{\mathrm{p}} \end{pmatrix}, \tag{2}$$

where $g_k = (1 + \mathrm{e}^{-\mathrm{i}k_x})\mathrm{e}^{\mathrm{i}k_y}$, $f_k = 1 - \mathrm{e}^{-\mathrm{i}k_x}$ and $\varepsilon_l = \mu_l + 2t_l \cos k_x + 2t_l' \cos(2k_x)$ $(l = \mathrm{p}, \mathrm{d})$ with the parameters $\mu_{\mathrm{d}} = 0.4935$, $\mu_{\mathrm{p}} = -1.3265$, $t_{\mathrm{d}} = -0.28$, $t_{\mathrm{d}}' = 0.075$, $t_{\mathrm{p}} = 0.93$, $t_{\mathrm{p}}' = 0.075$, $t_0^{\mathrm{AB}} = 1.02$, $t_{\mathrm{d}}^{\mathrm{AB}} = 0.52$, $t_{\mathrm{p}}^{\mathrm{AB}} = 0.4$ in units of eV. The SOC term is $V_{\mathrm{SOC}} = 0.115$.

Utilizing the TB Hamiltonian, we proceed to analyze the band structure under various terminations. We construct a lattice model with periodic boundary conditions in the x-direction and open boundary conditions in the y-direction with

a width $2W$. Accordingly, both the upper and lower edges of the slab in the x direction feature four distinct terminations denoted as $\mathrm{W(Te)}_i$ $(i = \mathrm{A,B})$. We represent the terminating atoms of the upper and lower edges using the set $[\mathrm{W(Te)}_i, \mathrm{W(Te)}_i]$. Theoretically, there are $4\times4 = 16$ potential configurations in total. Nevertheless, due to the inversion symmetry of the unit cell, $\mathrm{W(Te)_A}$ is equivalent to $\mathrm{W(Te)_B}$, resulting in redundant configurations, such as $[\mathrm{W_A,W_A}] = [\mathrm{W_B,W_B}]$, reducing the count to ten distinct cases (Appendix A). Figure 2(a) illustrates a representative band structure with termination $[\mathrm{W_A,W_B}]$ (inset in Fig. 2), which features degenerate edge states. This degeneracy arises from the inversion symmetry connecting the upper $\mathrm{W_A}$ atoms and the lower $\mathrm{W_B}$ atoms. In contrast, the band structure associated with the termination $[\mathrm{W_A,Te_B}]$ (Fig. 2(b)) displays non-degenerate edge states, where each edge exhibits different Fermi velocities owing to the non-equivalent terminating atoms. Additional band structures for various termination configurations are detailed in Appendix A.

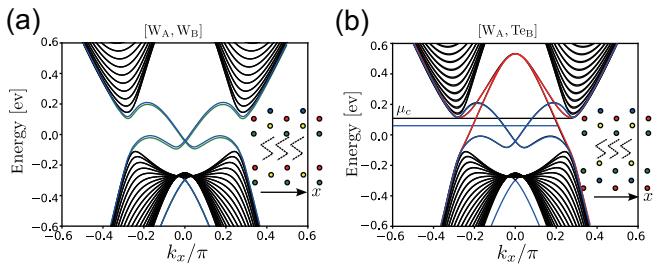


Fig. 2. (a)–(b) Band structure with the periodic condition in the x-direction, open boundary condition in the y-direction with the width of $W = 11$. (a) The band structure with the termination $[\mathrm{W_A,W_B}]$. (b) The band structure with the termination $[\mathrm{W_A,Te_B}]$, the edge states are colored the same as the edge atom. The blue horizontal line is the chemical potential in the bulk and used in Fig. 3, μ_c is the position of the bottom of the conduction band.

The scenarios vary when periodic boundary conditions are imposed in the y direction and open boundary conditions in the x direction with a length of $2L$. Within this framework, two distinct terminations, $\mathrm{W_ATe_A}$ and $\mathrm{W_BTe_B}$, exist for the two edges of the slab along the y direction. We represent these edge configurations with $[(\mathrm{WTe})_i, (\mathrm{WTe})_i]$. In principle, there are $2\times2 = 4$ possible configurations of the slab in total. Remarkably, all four configurations are equivalent due to mirror symmetry M_x, which relates the two edges in the $[(\mathrm{WTe})_i, (\mathrm{WTe})_i]$ termination, and inversion symmetry, which connects the edges in the $[(\mathrm{WTe})_i, (\mathrm{WTe})_{\bar{i}}]$ termination, with $\bar{i}$ denoting the opposite of i. The band structures display identical characteristics, featuring degenerate edge states with a Dirac point crossing at $k_y = \pi$[69] (Appendix A). Consequently, to implement the necessary asymmetry for the JDE, the Josephson junction must be constructed along the x direction.

3. JDE with edge distortion

We consider the JDE in $\mathrm{WTe_2}$ based Josephson junction, which is composed of a 2D $\mathrm{WTe_2}$ covered with superconductors on both ends. Given that the band structure along the y-direction presents symmetric edges due to inversion and mirror symmetries, we thus focus on the junction along the x-direction, as shown in Fig. 1(a). In the Nambu basis, the Bogoliubov–de Gennes (BdG) Hamiltonian of the system

$$H_{\mathrm{BdG}} = \begin{pmatrix} H_0(k) & \Delta \\ \Delta^\dagger & -H_0^*(-k) \end{pmatrix}. \tag{3}$$

Without loss of generality, we here consider the edges formed by $\mathrm{W_A}$ and $\mathrm{Te_B}$ atoms, with the associated band dispersion depicted in Fig. 2(b). Then, we construct a TB BdG Hamiltonian of SC/TI/SC junction with the $\mathrm{WTe_2}$ Hamiltonian Eq. (1) and compute the Andreev levels of the system by calculating the eigenenergies of the TB Hamiltonian as a function of the superconducting phase difference ϕ. The magnetic field is applied via the Peierls substitution.[74] With the Landau gauge $\boldsymbol{A} = (By, 0, 0)$, the hopping between site "1" coordinates $(x_1, y_1)a$ and site "2" coordinates $(x_2, y_2)a$ will change to $t \to t\,\mathrm{e}^{-\mathrm{i}e/\hbar\int_{(x_1,y_1)}^{(x_2,y_2)}\boldsymbol{A}\cdot\mathrm{d}l} = t\exp[\mathrm{i}\pi(x_2-x_1)\frac{(y_2+y_1)}{2}\frac{Ba^2}{\phi_0}]$. Notably, a 4π Josephson effect is anticipated in the ideal case with conserved fermion parity within a topological insulator-based Josephson junction. However, quasiparticle poisoning can induce fermion parity switches, leading to a 2π Josephson effect,[20,75] and we consider this scenario in our analysis.

When the Fermi level falls within the bulk gap (indicated by the blue line in Fig. 2(b)), only two edge states can facilitate Cooper pair tunneling. The mismatch in Fermi velocities (v_f) between the two edge states leads to differing coherence lengths ($\xi = \hbar v_\mathrm{f}/2\Delta$) for these states, $\xi_u \neq \xi_\mathrm{d}$. Consequently, the Andreev level originating from the top and bottom edges differs, as shown in Fig. 3(a). The junction, therefore, behaves effectively as two inequivalent Josephson junctions arranged in a SQUID-like configuration. The associated edge junction Andreev levels take the form[52,76,77]

$$E(\phi) = \pm\tilde{\Delta}\sqrt{1 - T\sin^2\left(\frac{\phi}{2}\right)}, \tag{4}$$

with T the transmission amplitude and $T \to 1$ for TI edge states.[77,78] $\tilde{\Delta}$ represents the eigenenergies of the junction at $\phi = 0$, which captures the junction length L and coherence length ξ and $\tilde{\Delta} = \Delta$ in the short junction limit $L/\xi \to 0$.[76] Due to time-reversal and particle-hole symmetries, the Andreev level energies approach zero when the phase difference $\phi = \pi$, which simplifies the spectrum to $E(\phi) = \pm\tilde{\Delta}|\cos(\phi/2)|$. With the perfect Andreev reflection in TI-based Josephson junctions,[78] the dependence of $\tilde{\Delta}$ on the junction length and coherence length is[79]

$$\left(\frac{\tilde{\Delta}}{\Delta}\right)\left(\frac{L}{\xi}\right) = 2\arccos\left(\frac{\tilde{\Delta}}{\Delta}\right), \tag{5}$$

with Δ the superconducting gap. The inset in Fig. 3(b) shows the dependence of $\tilde{\Delta}$ on the junction length. In the short junction limit, $L/\xi \to 0$, $\tilde{\Delta}$ approaches Δ, and the Andreev levels contributed by the two edges exhibit minimal differences. Thus, to capture the inversion symmetry breaking (asymmetric edge states), we anticipate the junction length to be small but not close to zero. Then, the asymmetric edge states lead to different $\tilde{\Delta}$, expressed as $\Delta_{1(2)}$. When an external magnetic field B is applied to the junction with effective area $S = w(d+2\lambda)$, with w, d, λ the junction width, length, and penetration depth. The Josephson potential of the system, contributed by the two asymmetric edges, can then be approximated as

$$V(\phi, \phi_B) = -\Delta_1 \left|\cos\left(\frac{\phi_1}{2}\right)\right| - \Delta_2 \left|\cos\left(\frac{\phi_2}{2}\right)\right|, \qquad (6)$$

where the two terms indicate the contributions of the two edges. $\phi_{1(2)}$ is the phase drop along the two edges. The phases are related through the magnetic flux threading the junction, $\phi_2 - \phi_1 = \phi_B$, where $\phi_B = 2\pi\phi_e/\phi_0$, $\phi_e = BS$ is the magnetic flux, and $\phi_0 = h/2e$ is the flux quantum. Note that asymmetric edge states acquire distinct additional phases due to the external magnetic flux, but these can be transformed into the form given in Eq. (6) through variable substitution and therefore do not affect the diode efficiency.

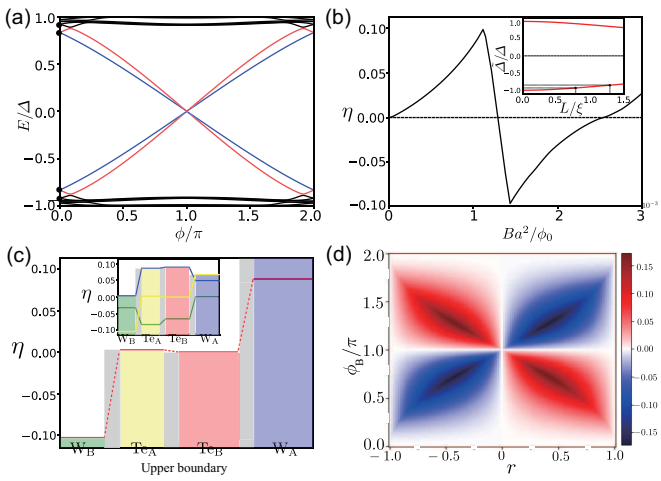


Fig. 3. (a) Andreev levels of the junction for $L = 20a$, with $L/\xi_{u(d)} \approx 0.83, 1.33$ for the two edge states, the two colors correspond to two edge states. The black dots at $\phi = 0$ correspond to the black dots in the inset in panel (b). (b) Diode efficiency changes with magnetic flux; the inset shows the Eigenenergies at $\phi = 0$ ($\tilde{\Delta}/\Delta$) change with junction length. (c) Diode efficiency as a function of the upper edge configuration while fixing the lower boundary atoms Te_B, at a constant magnetic flux $Ba^2/\Phi_0 \approx 1.11 * 10^{-3}$ (the maximal η in panel (b)). The inset shows the diode efficiency as a function of the upper edge configuration while fixing the lower boundary atoms W_A, W_B, Te_A. The lines' color corresponds to distinct lower boundary atoms, the colored regions indicate different upper boundary atom configurations, with colors matching Fig. 1. (d) Diode efficiency changes with asymmetric r and magnetic flux ϕ_B with the toy potential Eq. (6).

Then, based on the TB Hamiltonian, we calculated the zero-temperature Josephson potential $V(\phi)$ at different magnetic fields and further calculated the Josephson current $I(\phi) = \frac{2e}{\hbar}\frac{\partial V(\phi)}{\partial \phi}$. The positive (negative) critical current, $I_{c+(-)}$, corresponds to the maximum (minimum) value of the Josephson current. Finally, the diode efficiency $\eta = (I_{c+} - |I_{c-}|)/(I_{c+} + |I_{c-}|)$ is calculated and plotted as a function of magnetic field, as shown in Fig. 3(b). The JDE disappears with $\eta = 0$ at a certain magnetic field $Ba^2/\phi_0 \approx 1.28 * 10^{-3}$ (corresponding to π flux in the junction) and exhibits odd symmetry around this point. These properties can be verified with the toy potential Eq. (6). At $\phi_B = \pi$, the Josephson potential preserves the symmetry $V(\phi) = V(\pi - \phi)$, resulting in the absence of the JDE. Moreover, the Josephson potentials at $\phi_B = 2\pi - \phi_B'$ and $\phi_B = -\phi_B'$ are equivalent up to a phase shift $\phi \to \phi - \pi$. This transformation effectively reverses the magnetic flux direction, leading to opposite interference conditions between the two edge states and consequently reversing the critical currents and the diode efficiency. Notably, the asymmetric edge states break inversion symmetry in 1T′-WTe_2-based Josephson junctions and thereby give rise to the JDE. We subsequently analyze the diode efficiency as a function of different edge configurations while fixing the magnetic field at the maximal diode efficiency point in Fig. 3(b). We keep the lower boundary in the Te_B atomic configuration and vary the configuration of the upper boundary. The resulting diode efficiency is shown in Fig. 3(c). Clearly, no JDE appears when the two edges are related by inversion symmetry (additional configurations are presented in the inset of Fig. 3(c)), e.g., W_A and W_B edges, Te_A and Te_B edges. Additionally, the JDE polarity reverses if the mismatch in Fermi velocity between the two edges is reversed (depicted by the red and yellow lines in Fig. 3(c)).[49,80]

Utilizing the toy potential Eq. (6) and defining the asymmetric parameter $r \equiv (\Delta_1 - \Delta_2)/(\Delta_1 + \Delta_2)$, we calculate the phase diagram of diode efficiency as a function of r and magnetic flux ϕ_B, illustrated in Fig. 2(d). The diode efficiency is clearly an odd function of both r and ϕ_B around $r = 0$ and $\phi_B = \pi$, consistent with the numerical results. Note that the Josephson potential form in Eq. (6) cannot accurately describe the Josephson potential when the junction violates the short junction limit, $L/\xi \gg 1$; more results are shown in Appendix C. The maximal diode efficiency is limited to about 30%, consistent with similar devices with asymmetric edge states.[80]

Having established the JDE in the 1T′-WTe_2 edge interferometer, we now show how to enhance the diode efficiency further. When the chemical potential is situated in the gap ($\mu \lesssim \mu_c$), the Josephson potential is primarily dominated by edge states. However, as the chemical potential is adjusted into the bulk states (Fig. 2(b)), which can be achieved with a gate voltage in experiment,[81] contributions from both edge and bulk states significantly impact the potential. The Andreev levels of the system, when the chemical potential is within the bulk states without a magnetic field, are numerically calculated and depicted in Fig. 4(a), clearly illustrating the bulk

state's contribution to the Josephson potential.

Then, we compute the Josephson potential as a function of magnetic field and extract the positive and negative critical currents to obtain the diode efficiency. The resulting η traces for different chemical potentials are shown in Fig. 4(b). As the chemical potential varies (shown in Fig. 2(b)), the edge-state decay length — set by the chemical potential and the bulk gap — increases, causing the edge modes to penetrate deeper into the sample. Consequently, the effective area enclosed by the edge trajectories becomes explicitly chemical-potential dependent, and the magnetic field at which the diode efficiency vanishes ($\eta = 0$) shifts accordingly, as shown by the blue and yellow lines in Fig. 4(b). However, it remains an odd function of the magnetic field around $\eta = 0$ when the chemical potential is in the gap, $\mu \lesssim \mu_c$. As the Fermi surface is further regulated to the bulk states, the diode efficiency loses its odd symmetry for specific magnetic fields due to bulk-state contributions to the Josephson potential (Fig. 4(b)). The maximum efficiency of the diode can reach 53% and subsequently decreases with increasing chemical potential (Fig. 4(c)). Notably, adjusting the chemical potential simultaneously modulates both the edge-state Fermi-velocity mismatch (Fig. 2(a)) and the count of transport channels and their Fermi velocities of bulk transport channels. In addition, as the chemical potential approaches the bottom of the conducting band, the junction no longer conforms to the short junction limit due to low Fermi velocities of the edge and bulk states. In this regime, the Josephson potential should be expressed in a Fourier series as

$$V'(\phi,\phi_B) = \sum_n E_{J\alpha}^{(n)}(\phi_B)\cos(n\phi) + E_{J\beta}^{(n)}(\phi_B)\sin(n\phi), \quad (7)$$

where $E_{J\alpha(\beta)}^{(n)}$ are the coefficients of the cosine and sine terms, respectively, and n labels the Fourier order. Note that the $\sin n\phi$ components arise predominantly from the asymmetric edges. Using the computed Josephson potential, we extract these coefficients as functions of magnetic flux for $\mu = 0.06$ (indicating low diode efficiency with chemical potential in the bulk gap) and $\mu = 0.14$ (achieving maximal diode efficiency with chemical potential in the bulk states), as shown in Fig. 4(d). The coefficients exhibit periodic variations with magnetic flux when the chemical potential is within the bulk gap (the dashed lines in Fig. 4(d)), consistent with the periodicity of the diode efficiency in Fig. 4(b) and Fig. 3(b). By contrast, this periodicity is lost due to bulk-state contributions when the chemical potential is tuned into the bulk states. Moreover, Fig. 4(d) shows a clear enhancement of both $E_{J\alpha}^{(n)}$ and $E_{J\beta}^{(n)}$, attributed to bulk transport channels and increased edge asymmetry, which together are responsible for the large diode efficiency. Notably, the bulk contribution depends not only on the chemical potential but also on the junction width (w), whereas the edge-induced asymmetry is largely width-independent. Consequently, the chemical potential that maximizes the diode efficiency depends on w rather than being universal. Finally, the enhancement of diode performance via bulk participation in the presence of substantial edge asymmetry is a robust and generic feature, as corroborated by the toy model in Appendix D.

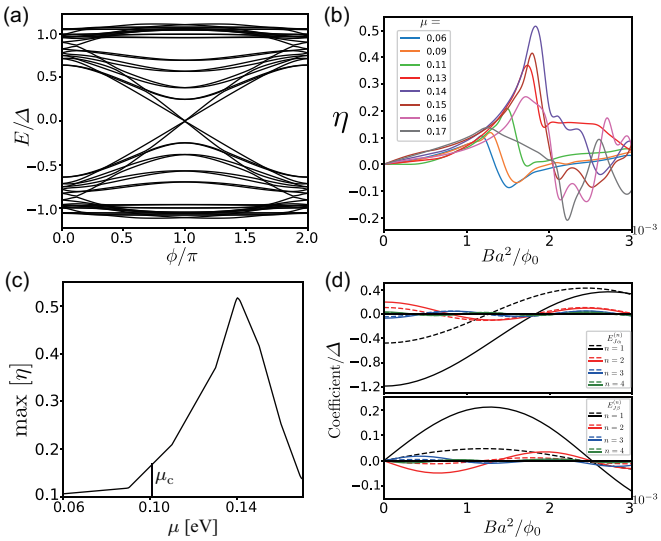


Fig. 4. (a) Andreev levels of the junction with a chemical potential in the bulk and slightly larger than μ_c, $\mu = 0.13$. (b) Diode efficiency changes with magnetic flux at different chemical potentials, changing from the gap ($\mu < \mu_c$) to the bulk state ($\mu > \mu_c$). (c) The maximal diode efficiency changes with chemical potential, extracted from (b), μ_c is the position of the bottom of the conduction band. (d) The Fourier coefficients as a function of magnetic flux with the chemical potential at $\mu = 0.06$ (the dashed lines) and $\mu = 0.14$ (the solid lines); the upper panel shows the coefficient of the cosine term; the lower panel shows the coefficient of the sine term.

However, the edges of the samples in experiments on 2D monolayer materials may be irregular, i.e., they have cracks, steps, or bumps.[82] Hence, such samples lose translational invariance along their boundaries, resulting in a variable Fermi velocity mismatch between the two edges, which further influences the JDE within the system. Here, we model a rough edge by the boundary following a random step δy appearing at each site along an initially translationally invariant boundary, where δy is randomly and uniformly distributed within the range of $[-\delta p, \delta p]$ and exhibits a zero mean, and the parameter δp characterizes the degree of boundary irregularity. In our numerical calculation, we take $\delta p = 0.4 b_y$ with b_y the unit length along y direction. Figure 5(a) illustrates an irregular system, which permits the addition or removal of up to one site along the boundary. This value suffices for experimentation as an atomically flat interface can be realized[44,49] and the short junction length (on the order of nanometers). With the rough edge system, we calculate the variations in Josephson diode efficiency with magnetic flux when the Fermi level is situated within the bulk gap and bulk states, as depicted in Fig. 5(b). The rough edge exerts minimal impact on diode efficiency when the Fermi level resides in the bulk gap. However, it significantly influences the performance when the Fermi level is

positioned at the bottom of the conduction band due to the low Fermi velocities of edge and bulk states. Nonetheless, a high diode efficiency is maintained when the Fermi level is in the bulk gap.

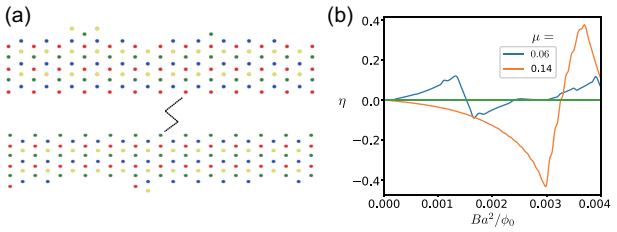


Fig. 5. (a) Geometries of the system with rough edges, corresponding to adding or removing two sites along the boundary randomly. (b) The diode efficiency as a function of magnetic flux with the rough edges shown in panel (a).

4. Discussion and summary

In this study, we have systematically investigated the Josephson diode effect in a junction based on monolayer 1T′-WTe_2. Our central results demonstrate that the intrinsic asymmetric edge terminations of WTe_2 nanoribbons provide a powerful resource for engineering a JDE. While the effect driven by topological edge states alone is significant, we have uncovered a crucial mechanism to further enhance the diode efficiency: tuning the chemical potential to allow for the participation of bulk states. This interplay boosts the maximum efficiency to more than 50%, a highly competitive value.

While the TB model in the main text captures the essential physics and is widely used for 1T′-WTe_2,[69–71] it has been shown that a more detailed model including additional spin–orbit coupling terms might be needed for a precise quantitative comparison with experiments.[83] Nevertheless, the core mechanism — the existence of inequivalent edge states — is a robust feature of WTe_2, and we expect our main conclusions to hold. Excitingly, with recent experimental advances in realizing gate-induced superconductivity in WTe_2 flakes,[81] our proposed device could potentially be implemented in an all-in-one material platform using local gating techniques, avoiding complex fabrication of hybrid structures.

In conclusion, our work establishes a novel route toward achieving a highly efficient and robust JDE. The gate-controlled technology can enhance the diode efficiency in an experiment. The principle of enhancing diode efficiency by admixing bulk transport channels is general and could be applied to other topological materials with asymmetric edge states,[20] such as $Ta_2Pd_3Te_5$[49] and $MnBi_2Te_4$.[41,42] These findings are not only of fundamental interest but also pave the way for the development of next-generation dissipationless quantum electronics.

Appendix A: Numerical calculation

For the numerical calculations, we construct the tight-binding models using the "KWANT" program[84] with the Hamiltonian in Eq. (1) to obtain the band structure with different edge terminations. For band structures along the x direction, the system is constructed with periodic conditions along the x direction, open boundary conditions along the y direction, with the transverse coordinate spanning $y \in [-W, W]$. For the band structures along the y direction, the system is constructed with periodic conditions along the y direction and open boundary conditions along the x direction, with the length range $x \in [-L, L]$. To gain different terminal configurations, the length or the width is fine-tuned within the corresponding ranges. For the numerical calculation of Josephson junction, we construct the tight-binding models by "KWANT" program[84] with the BdG Hamiltonian in Eq. (3). The junction length is $d = 20a$, width is $w = 22a$, and the coherent lengths for the two edge states are $\xi_{u(d)} = 15a, 25a$ in Fig. 3(a). The Andreev levels are obtained by calculating the eigenenergies of the TB Hamiltonian as a function of phase difference ϕ, and the zero temperature free energy (also the Josephson potential $V(\phi)$) is obtained by summing all negative eigenenergies. With the Josephson potential, we can get the current-phase relation, $I(\phi) = \frac{2e}{\hbar}\frac{\partial V(\phi)}{\partial \phi}$. The critical currents are the maximal and minimal currents in the current-phase relation. The perpendicular magnetic field is applied via Perierls substitution.[74] With the Landau gauge $\boldsymbol{A} = (By, 0, 0)$, the hopping between site "1" coordinates $(x_1, y_1)a$ and site "2" coordinates $(x_2, y_2)a$ will change to $t \to t\, e^{-ie/\hbar \int_{(x_1,y_1)}^{(x_2,y_2)} \boldsymbol{A}\cdot dl} = t \exp[i\pi(x_2 - x_1)\frac{(y_2+y_1)}{2}\frac{Ba^2}{\phi_0}]$.

Appendix B: Band structure of WTe_2

Here, we demonstrate the band structure of the WTe_2 slab along the x-direction. There are a possible $4 \times 4 = 16$ configurations of the slab along the x-direction in total. However, due to the inversion symmetry of the unit cell, there are only ten unique configurations. The redundancies can be noted as follows $[W_A, W_A] = [W_B, W_B]$, $[W_A, Te_A] = [Te_B, W_B]$, $[W_A, Te_B] = [Te_A, W_B]$, $[Te_A, W_A] = [W_B, Te_B]$, $[Te_A, Te_A] = [Te_B, Te_B]$, $[W_B, Te_A] = [Te_B, W_A]$. The complete band structure for all 16 terminal configurations is depicted in Fig. B1, where equivalent cases are clearly identified.

With the periodic boundary condition in the y direction, the band structures are shown in Fig. B2. There are possible $2 \times 2 = 4$ configurations of the slab along the y-direction in total. However, due to the inversion symmetry of the unit cell and the mirror symmetry M_y of the slab along the y direction, all the band structures are equivalent. Figure B2 shows the band structures with terminations $[(WTe)_A, (WTe)_A]$ and $[(WTe)_A, (WTe)_B]$, displaying identical characteristics.

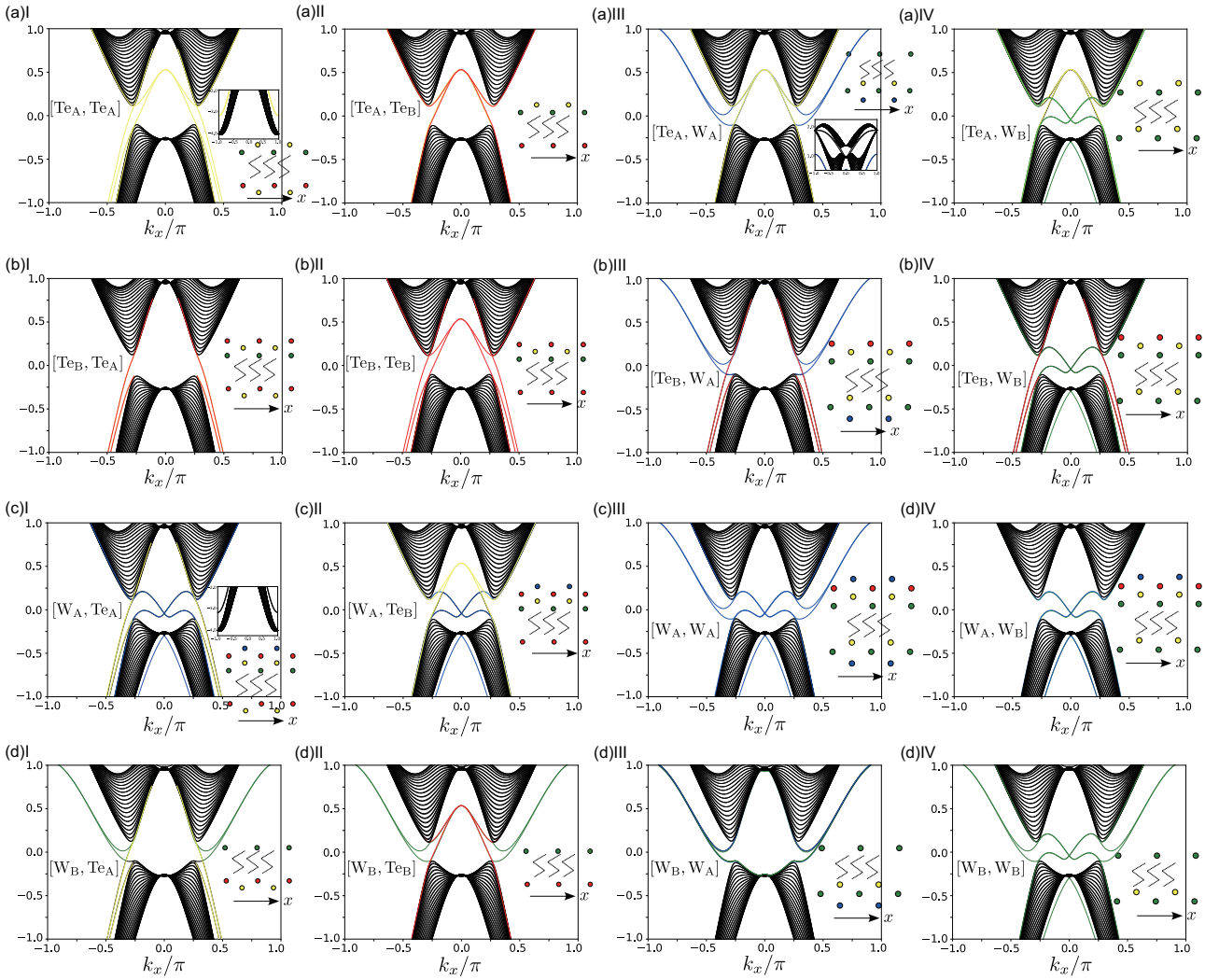


Fig. B1. With periodic condition in x direction and width $W = 11$. Band structures of all 16 terminal configurations. The inset shows the configuration of the terminations.

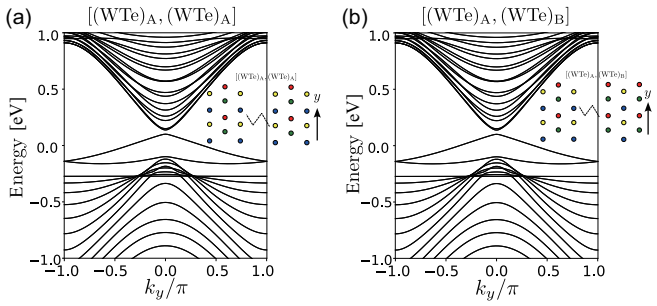


Fig. B2. Band structure with the periodic condition in the y-direction, open boundary condition in the x-direction with the length of $L = 15$, with terminations $[(\mathrm{WTe})_\mathrm{A}, (\mathrm{WTe})_\mathrm{A}]$ (a) and $[(\mathrm{WTe})_\mathrm{A}, (\mathrm{WTe})_\mathrm{B}]$ (b). Insets show the structure for the terminations $[(\mathrm{WTe})_\mathrm{A}, (\mathrm{WTe})_\mathrm{A}]$ and $[(\mathrm{WTe})_\mathrm{A}, (\mathrm{WTe})_\mathrm{B}]$, the two edges of the termination $[(\mathrm{WTe})_\mathrm{A}, (\mathrm{WTe})_\mathrm{A}]$ are related by the M_x symmetry (the dashed green line).

Appendix C: Diode efficiency changes with magnetic flux with the chemical potential in the gap

Here, we present additional results on diode efficiency as a function of magnetic flux, with the chemical potential located within the gap. Adjusting the chemical potential alters the mismatch in the Fermi velocity of the edge states, consequently modifying the coherence length of these states. When the junction exceeds the short junction limit $L/\xi \gg 1$, the Josephson potential cannot be accurately approximated using the form in Eq. (6). Instead, it can be represented by the Fourier series in Eq. (7). Figure C1(a) illustrates the band structure alongside the chemical potential configuration where the junction length L notably exceeds the coherence length ξ.

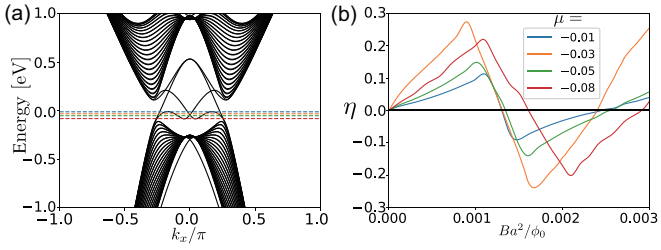


Fig. C1. Diode efficiency as a function of magnetic flux with the chemical potential in the gap. (a) The band structure and (b) the diode efficiency as a function of magnetic flux with different chemical potentials in Panel (a).

Figure C1(b) depicts the diode efficiency as a function of magnetic flux with the chemical potential marked in panel (a). The maximum diode efficiency reaches approximately 30%.[23,36]

Appendix D: Diode effect with toy Josephson potential

In the 2DTI-based Josephson junction, the asymmetric edges and magnetic flux play a crucial role in generating the JDE, with diode efficiency primarily constrained by the asymmetry of the edges alone. However, when Josephson currents contributed by bulk states are considered, diode efficiency can be significantly enhanced. To further establish the universality of this conclusion, we consider the ideal scenario in which the junction adheres to the short junction limit for edge states, and bulk states conform to the Fraunhofer diffraction pattern averaged over magnetic flux. This scenario differs from that considered in the main text, where the short-junction limit is violated and only a few bulk channels participate. The toy model for the Josephson potential can then be written as

$$V'(\phi,\phi_{\rm B}) = -\Delta_1\left|\cos\left(\frac{\phi_1}{2}\right)\right| - \Delta_2\left|\cos\left(\frac{\phi_2}{2}\right)\right| - E_b\cos\phi\frac{\sin(k_3\phi_{\rm B})}{(k_3\phi_{\rm B})}, \tag{D1}$$

where $E_b > 0$ is the amplitude of the Josephson potential contributed by bulk states, and can be tuned by the chemical potential. $\phi_{1(2)} = \phi + k_{1(2)}\phi_{\rm B}/2$ and $k_{1,2,3}$ characterize the phases of the edge states and bulk states due to magnetic flux. Because asymmetric edges with different Fermi velocities have different decay lengths and critical Josephson currents, the Josephson potentials contributed by the two edges acquire different additional phases in the presence of magnetic flux ($k_1 \neq k_2$). Consequently, in the presence of bulk-state contributions, the Josephson potential cannot in general be reduced to the form of Eq. (6). Moreover, due to the finite decay length of the edge states, the area enclosed by the edge trajectories is slightly smaller than the geometric junction area. As a result, the magnetic flux enclosed by the junction area does not exactly correspond to the phase differences accumulated by the two edge states, meaning that $(k_1+k_2)/2$ is not strictly equal to k_3. However, in experiments, we expect the junction width to be significantly larger than the decay length of edge states. Therefore, we roughly approximate $k_1 \approx k_2 \approx k_3 = 1$ to explore the enhancement of diode efficiency with bulk states. By fixing Δ_1 and defining the asymmetry parameter $r \equiv (\Delta_1-\Delta_2)/(\Delta_1+\Delta_2)$, we calculate the maximal diode efficiency as a function of r and E_b, shown in Fig. D1. The results clearly demonstrate that the inclusion of bulk-state contributions can significantly enhance the maximal diode efficiency in the presence of strong edge asymmetry.

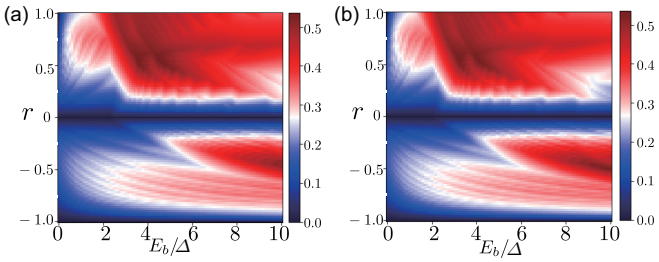


Fig. D1. The maximal diode efficiency changes with r and E_b with the toy potential Eq. (D1) with $k_1 \approx k_2 \approx k_3 = 1$. (a) and (b) are the results with $\Delta_1 = 0.85\Delta, 0.95\Delta$, respectively.

Acknowledgments

We acknowledge useful discussions with Noah F. Q. Yuan, Shun Wang, and Cheng-Yu Yan. Project supported by the Innovation Program for Quantum Science and Technology (Grant No. 2021ZD0302700), the National Natural Science Foundation of China (NSFC) (Grant No. 12074133), the Shanghai Science and Technology Innovation Action Plan (Grant No. 24LZ1400800), and the Project supported by Cultivation Project of Shanghai Research Center for Quantum Sciences (Grant No. LZPY2024).

References

[1] Scaff J H and Ohl R S 1947 *Bell Syst. Tech. J.* **26** 1
[2] Shockley W 1949 *Bell Syst. Tech. J.* **28** 435
[3] Jiang K and Hu J 2022 *Nat. Phys.* **18** 1145
[4] Jiang X, Connolly P J, Hagen S J and Lobb C J 1994 *Phys. Rev. B* **49** 9244
[5] Braginski A I 2019 *J. Supercond. Nov. Magn.* **32** 23
[6] Ando F, Miyasaka Y, Li T, Ishizuka J, Arakawa T, Shiota Y, Moriyama T, Yanase Y and Ono T 2020 *Nature* **584** 373
[7] Miyasaka Y, Kawarazaki R, Narita H, Ando F, Ikeda Y, Hisatomi R, Daido A, Shiota Y, Moriyama T, Yanase Y and Ono T 2021 *Appl. Phys. Express* **14** 073003
[8] Zhang Y, Gu Y, Li P, Hu J and Jiang K 2022 *Phys. Rev. X* **12** 041013
[9] He J J, Tanaka Y and Nagaosa N 2022 *New J. Phys.* **24** 053014
[10] Tanaka Y, Lu B and Nagaosa N 2022 *Phys. Rev. B* **106** 214524
[11] Bauriedl L, Bäuml C, Fuchs L, Baumgartner C, Paulik N, Bauer J M, Lin K Q, Lupton J M, Taniguchi T, Watanabe K, Strunk C and Paradiso N 2022 *Nat. Commun.* **13** 4266
[12] Liang W, Zeng J, Qiao Z, Gao Y and Niu Q 2023 *Phys. Rev. Lett.* **131** 256901
[13] de Picoli T, Blood Z, Lyanda-Geller Y and Väyrynen J I 2023 *Phys. Rev. B* **107** 224518
[14] Satchell N, Shepley P, Rosamond M and Burnell G 2023 *J. Appl. Phys.* **133** 203901
[15] Hou Y, Nichele F, Chi H, Lodesani A, Wu Y, Ritter M F, Haxell D Z, Davydova M, Ilić S, Glezakou-Elbert O, Varambally A, Bergeret F S, Kamra A, Fu L, Lee P A and Moodera J S 2023 *Phys. Rev. Lett.* **131** 027001
[16] Banerjee S and Scheurer M S 2024 *Phys. Rev. Lett.* **132** 046003
[17] Debnath D and Dutta P 2024 *Phys. Rev. B* **109** 174511
[18] Yu Y, Han S, Chu X, Chu S I and Wang Z 2002 *Science* **296** 889
[19] Ioffe L B, Geshkenbein V B, Feigel'man M V, Fauchère A L and Blatter G 1999 *Nature* **398** 679
[20] Chen C Z, He J J, Ali M N, Lee G H, Fong K C and Law K T 2018 *Phys. Rev. B* **98** 075430
[21] Baumgartner C, Fuchs L, Costa A, Reinhardt S, Gronin S, Gardner G C, Lindemann T, Manfra M J, Faria Junior P E, Kochan D, Fabian J, Paradiso N and Strunk C 2022 *Nat. Nanotechnol.* **17** 39
[22] Davydova M, Prembabu S and Fu L 2022 *Sci. Adv.* **8** eabo0309
[23] Pal B, Chakraborty A, Sivakumar P K, Davydova M, Gopi A K, Pandeya A K, Krieger J A, Zhang Y, Date M, Ju S, Yuan N, Schröter N B M, Fu L and Parkin S S P 2022 *Nat. Phys.* **18** 1228

[24] Steiner J F, Melischek L, Trahms M, Franke K J and von Oppen F 2023 *Phys. Rev. Lett.* **130** 177002
[25] Banerjee A, Geier M, Rahman M A, Thomas C, Wang T, Manfra M J, Flensberg K and Marcus C M 2023 *Phys. Rev. Lett.* **131** 196301
[26] Legg H F, Laubscher K, Loss D and Klinovaja J 2023 *Phys. Rev. B* **108** 214520
[27] Maiani A, Flensberg K, Leijnse M, Schrade C, Vaitiekėnas S and Seoane Souto R 2023 *Phys. Rev. B* **107** 245415
[28] Yokoyama T, Eto M and Nazarov Y V 2014 *Phys. Rev. B* **89** 195407
[29] Alidoust M, Shen C and Zutić I 2021 *Phys. Rev. B* **103** L060503
[30] Yuan N F Q and Fu L 2022 *Proc. Natl. Acad. Sci. USA* **119** e2119548119
[31] Legg H F, Loss D and Klinovaja J 2022 *Phys. Rev. B* **106** 104501
[32] Jeon K R, Kim J K, Yoon J, Jeon J C, Han H, Cottet A, Kontos T and Parkin S S P 2022 *Nat. Mater.* **21** 1008
[33] Lu B, Ikegaya S, Burset P, Tanaka Y and Nagaosa N 2023 *Phys. Rev. Lett.* **131** 096001
[34] Turini B, Salimian S, Carrega M, Iorio A, Strambini E, Giazotto F, Zannier V, Sorba L and Heun S 2022 *Nano Lett.* **22** 8502
[35] He J J, Tanaka Y and Nagaosa N 2023 *Nat. Commun.* **14** 3330
[36] Guo G L, Pan X H and Liu X 2025 *Phys. Rev. B* **112** 014509
[37] Yun J, Son S, Shin J, Park G, Zhang K, Shin Y J, Park J G and Kim D 2023 *Phys. Rev. Res.* **5** L022064
[38] Lin J X, Siriviboon P, Scammell H D, Liu S, Rhodes D, Watanabe K, Taniguchi T, Hone J, Scheurer M S and Li J I A 2022 *Nat. Phys.* **18** 1221
[39] Díez-Mérida J, Díez-Carlón A, Yang S Y, Xie Y M, Gao X J, Senior J, Watanabe K, Taniguchi T, Lu X, Higginbotham A P, Law K T and Efetov D K 2023 *Nat. Commun.* **14** 2396
[40] Hu J X, Sun Z T, Xie Y M and Law K T 2023 *Phys. Rev. Lett.* **130** 266003
[41] Gao A, Chen S W, Ghosh B, Qiu J X, Liu Y F, Onishi Y, Hu C, Qian T, Bérubé D, Dinh T, Li H, Tzschaschel C, Park S, Huang T, Lien S W, Sun Z, Ho S C, Singh B, Watanabe K, Taniguchi T, Bell D C, Bansil A, Lin H, Chang T R, Yacoby A, Ni N, Fu L, Ma Q and Xu S Y 2024 *Nat. Electron.* **7** 751
[42] Zhang E, Sun Z T, Jia Z, Yang J, Yan J, Ai L, Xie Y M, Zhang Y, Gao X J, Xu X, Liu S, Ma Q, Hu C, Kou X, Zou J, Ni N, Law K T, Dong S and Xiu F 2025 *Sci. Adv.* **11** eads8730
[43] Qi S, Ge J, Ji C, Ai Y, Ma G, Wang Z, Cui Z, Liu Y, Wang Z and Wang J 2025 *Nat. Commun.* **16** 531
[44] Zhu Y, Wang H, Wang Z, Hu S, Gu G, Zhu J, Zhang D and Xue Q K 2023 *Phys. Rev. B* **108** 174508
[45] Ghosh S, Patil V, Basu A, Kuldeep, Dutta A, Jangade D A, Kulkarni R, Thamizhavel A, Steiner J F, von Oppen F and Deshmukh M M 2024 *Nat. Mater.* **23** 612
[46] Souto R S, Leijnse M and Schrade C 2022 *Phys. Rev. Lett.* **129** 267702
[47] Haenel R and Can O 2022 arXiv:2212.02657 [cond-mat.supr-con]
[48] Paolucci F, De Simoni G and Giazotto F 2023 *Appl. Phys. Lett.* **122** 042601
[49] Li Y, Yan D, Hong Y, Sheng H, Wang A, Dou Z, Guo X, Shi X, Su Z, Lyu Z, Qian T, Liu G, Qu F, Jiang K, Wang Z, Shi Y, Xu Z A, Hu J, Lu L and Shen J 2024 *Nat. Commun.* **15** 9031
[50] Gingrich E C, Niedzielski B M, Glick J A, Wang Y, Miller D L, Loloee R, Pratt Jr W P and Birge N O 2016 *Nat. Phys.* **12** 564
[51] Szombati D B, Nadj-Perge S, Car D, Plissard S R, Bakkers E P A M and Kouwenhoven L P 2016 *Nat. Phys.* **12** 568
[52] Krempasky J, Smejkal L, D'Souza S W, *et al.* 2024 *Nature* **626** 517
[53] Liu Y, Yu J and Liu C C 2024 *Phys. Rev. Lett.* **133** 206702
[54] Fu L and Kane C L 2009 *Phys. Rev. B* **79** 161408
[55] Badiane D M, Houzet M and Meyer J S 2011 *Phys. Rev. Lett.* **107** 177002
[56] Cho S, Dellabetta B, Yang A, Schneeloch J, Xu Z, Valla T, Gu G, Gilbert M J and Mason N 2013 *Nat. Commun.* **4** 1689
[57] Oostinga J B, Maier L, Schüffelgen P, Knott D, Ames C, Brüne C, Tkachov G, Buhmann H and Molenkamp L W 2013 *Phys. Rev. X* **3** 021007
[58] Wei Y J, Liu H L, Wang J and Liu J F 2022 *Phys. Rev. B* **106** 165419
[59] Wang J, Jiang Y, Wang J J and Liu J F 2024 *Phys. Rev. B* **109** 075412
[60] Kheirkhah M, Zhu D, Maciejko J and Yan Z 2022 *Phys. Rev. B* **106** 085420
[61] Zhu D, Kheirkhah M and Yan Z 2023 *Phys. Rev. B* **107** 085407
[62] Qian X, Liu J, Fu L and Li J 2014 *Science* **346** 1344
[63] Deng K, Wan G, Deng P, Zhang K, Ding S, Wang E, Yan M, Huang H, Zhang H, Xu Z, Denlinger J, Fedorov A, Yang H, Duan W, Yao H, Wu Y, Fan S, Zhang H, Chen X and Zhou S 2016 *Nat. Phys.* **12** 1105
[64] Ritschel T, Trinckauf J, Koepernik K, Büchner B, Zimmermann M v, Berger H, Joe Y I, Abbamonte P and Geck J 2015 *Nat. Phys.* **11** 328
[65] Li L J, O'Farrell E C T, Loh K P, Eda G, Özyilmaz B and Castro Neto A H 2016 *Nature* **529** 185
[66] Yuan N F Q, Mak K F and Law K T 2014 *Phys. Rev. Lett.* **113** 097001
[67] Lu J M, Zheliuk O, Leermakers I, Yuan N F Q, Zeitler U, Law K T and Ye J T 2015 *Science* **350** 1353
[68] Xi X, Wang Z, Zhao W, Park J H, Law K T, Berger H, Forró L, Shan J and Mak K F 2016 *Nat. Phys.* **12** 139
[69] Ok S, Muechler L, Di Sante D, Sangiovanni G, Thomale R and Neupert T 2019 *Phys. Rev. B* **99** 121105
[70] Hsu Y T, Cole W S, Zhang R X and Sau J D 2020 *Phys. Rev. Lett.* **125** 097001
[71] Nandy S and Pesin D A 2022 *SciPost Phys.* **12** 120
[72] Choe D H, Sung H J and Chang K J 2016 *Phys. Rev. B* **93** 125109
[73] Muechler L, Alexandradinata A, Neupert T and Car R 2016 *Phys. Rev. X* **6** 041069
[74] Datta S 1995 *Electronic Transport in Mesoscopic Systems* (Cambridge: Cambridge University Press)
[75] Pribiag V S, Beukman A J A, Qu F, Cassidy M C, Charpentier C, Wegscheider W and Kouwenhoven L P 2015 *Nat. Nanotechnol.* **10** 593
[76] Beenakker C W J 1991 *Phys. Rev. Lett.* **67** 3836
[77] Guo G L, Leng H B and Liu X 2024 *New J. Phys.* **26** 063005
[78] König M, Buhmann H, Molenkamp L W, Hughes T, Liu C X, Qi X L and Zhang S C 2008 *J. Phys. Soc. Jpn.* **77** 031007
[79] Schäpers T 2001 *Superconductor/Semiconductor Junctions* (Berlin: Springer)
[80] Nikodem E, Schluck J, Geier M, Papaj M, Legg H F, Feng J, Bagchi M, Fu L and Ando Y 2024 arXiv:2412.16569 [cond-mat.supr-con]
[81] Sajadi E, Palomaki T, Fei Z, Zhao W, Bement P, Olsen C, Luescher S, Xu X, Folk J A and Cobden D H 2018 *Science* **362** 922
[82] Wu S, Fatemi V, Gibson Q D, Watanabe K, Taniguchi T, Cava R J and Jarillo-Herrero P 2018 *Science* **359** 76
[83] Lau A, Ray R, Varjas D and Akhmerov A R 2019 *Phys. Rev. Mater.* **3** 054206
[84] Groth C W, Wimmer M, Akhmerov A R and Waintal X 2014 *New J. Phys.* **16** 063065